# Imaging and modelling the impact of multi-scale pore connectivity on two-phase flow in mixed-wet rock

Shan Wang[1,2], Arjen Mascini[1,2], Leonardo C. Ruspini[3], Pål-Eric Øren[3] and Tom Bultreys[1,2]

[1]Department of Geology, Pore-Scale Processes in Geomaterials Research (PProGRess), Ghent University, Krijgslaan 281/S8, B-9000, Ghent, Belgium

[2]Centre for X-ray Tomography (UGCT), Ghent University, Proeftuinstraat 86, B-9000, Ghent, Belgium

[3]Petricore Norway A.S., Trondheim, Norway

Corresponding author: Shan Wang (Shan.Wang@UGent.be)

**Key Points:**

- We observe quasi-stable meniscus movements on mixed-wet sample that differ from the conventional capillary-driven filling behavior.
- We quantify the fluid saturation in micrometer scale porosity to investigate how connectivity and wettability impact the displacements.
- A multi-scale pore network model is used to interpret the imaging experiments.

**Abstract**

The wetting properties of pore walls have a strong effect on multiphase flow through porous media. However, the fluid flow behaviour in porous materials with both complex pore structures and non-uniform wettability are still unclear. Here, we performed unsteady-state quasi-static oil- and waterflooding experiments to study multiphase flow in two sister heterogeneous sandstones with variable wettability conditions (i.e. one natively water-wet and one chemically treated to be mixed-wet). The pore-scale fluid distributions during this process were imaged by laboratory-based X-ray micro-computed tomography (micro-CT). In the mixed-wet case, we observed pore filling events where the fluid interface appeared to be at quasi-equilibrium at every position along the pore body (13% by volume), in contrast to capillary instabilities typically associated with slow drainage or imbibition. These events corresponded to slow displacements previously observed in unsteady-state experiments, explaining the wide range of displacement time scales in mixed-wet samples. Our new data allowed us to quantify the fluid saturations below the image resolution, indicating that slow events were caused by the presence of microporosity and the wetting heterogeneity. Finally, we investigated the sensitivity of the multi-phase flow properties to the slow filling events using a state-of-the-art multi-scale pore network model. This indicated that pores where such events took place contributed up to 19% of the sample's total absolute permeability, but that the impact on the relative permeability may be smaller. Our study sheds new light on poorly understood multiphase fluid dynamics in complex rocks, of interest to e.g. groundwater remediation and subsurface $CO_2$ storage.

## 1 Introduction

Immiscible two-phase flow through porous media is very common in natural subsurface systems. A thorough understanding of fluid flow mechanisms has crucial applications in geological $CO_2$ sequestration (Shukla et al., 2010), contaminated groundwater remediation (Kalhor et al., 2019) and subsurface energy storage (Panfilov, 2010). In recent years, in order to better characterize the intricate internal pore structures of porous materials, advanced imaging techniques such as X-ray micro-computed tomography (micro-CT) have been widely applied in the laboratory (Chen et al., 2021; Gao et al., 2019; Iglauer et al., 2011; Lin et al., 2021; Offenwert et al., 2019). The combination of X-ray micro-CT imaging with flow experiments has greatly facilitated the study of multiphase flow behavior at the pore scale. High-resolution images can provide important information to quantify the flow properties including fluid distributions (Lin et al., 2021), fluid flow dynamics (Reynolds et al., 2017; Singh et al., 2022; Spurin et al., 2019), filling characteristics (Bultreys et al., 2018; Gao et al., 2020), interfacial properties (Garing et al., 2017; Herring et al., 2017; Zankoor et al., 2021), etc., which cannot be measured in traditional core flooding experiments.

Wettability is known to play a crucial role in multiphase flow through porous rocks. It controls the fluid invasion sequences and the fluid distribution state in the pore network, which in turn influences the constitutive properties used in continuum models, for example capillary pressure and relative permeability. While most minerals are water-wet, the adhesion of surface active components present in e.g. crude oil or certain environmental pollutants can lead to changes in the fluid affinity to the surface, i.e. wettability alteration (Al-Futaisi & Patzek, 2004; Buckley et al., 1998; Gao et al., 2020; Morrow, 1990). For example, in a mixed-wet system pore surfaces in larger pores become hydrophobic due to direct contact with surface active components, while corners, crevices and smaller pores retain water and therefore remain more hydrophilic. This is influenced by a number of factors, including surface roughness, pore morphology, mineral composition, etc. (AlRatrout et al., 2018b; Garfi et al., 2020). At the pore scale, the resulting wettability alteration is reflected by changes in local contact angles. Recent advances in image processing algorithms have made it possible to quantify this directly on 3D images of the fluid

distribution (Andrew et al., 2014; Klise et al., 2016; Scanziani et al., 2017). The contact angle measured on segmented images is usually termed the “geometric contact angle” in literature (Alhammadi et al., 2020). This calculation can be done either manually or automatically. More recently, the thermodynamic contact angle (Blunt et al., 2019), event-based contact angle (Mascini et al., 2020), force-based contact angle (Mascini et al., 2020) and topology-based contact angle (Sun et al., 2020) were proposed to reduce the uncertainty of measuring contact angles during a displacement process.

Although significant progress has been achieved in revealing complex fluid dynamics in porous media based on advanced imaging techniques, most research has focused on materials with homogeneous wettability (mostly water-wet state) and simple pore structures (Berg et al., 2013; Datta et al., 2014; Offenwert et al., 2019; Rücker et al., 2015). The fluid flow mechanisms in heterogeneous rocks with non-uniform wetting, in which the pore sizes span from a few nanometers to centimeter scale, are still poorly understood. Alhammadi et al. (2020) and Lin et al. (2021) performed co-injection experiments to measure relative permeability in altered-wettability carbonate samples, but the macroscopic capillary pressure cannot be obtained from this type of experiments. Mascini et al. (2021) recently reported a newly discovered fluid invasion phenomenon in a rock with both structural and wetting heterogeneity: a significant proportion of the pore-scale fluid displacements were observed to be several orders of magnitude slower than the traditional displacement types found in neighboring pores (e.g. Haines jumps). They hypothesized that the complex wettability and pore space architecture changed the local capillary-viscous force balance, which could be the main reason for the concurrence of these slow filling events and fast displacements. However, they only showed the fluid dynamics during waterflooding, and couldn’t fully relate the behavior to the effects of microporosity (i.e. the porosity for pores below image resolution). To further explain what causes this filling behavior and how important it is in slow flooding, it is necessary to develop a comprehensive experimental and simulation workflow to study the underlying mechanisms of multiphase flow in geological rocks with complex wettability and pore structures.

In this paper, we introduce an experimental procedure that uses both oil-wet and water-wet

porous plates to perform unsteady-state capillary oil and waterflooding on heterogeneous sandstone samples in water-wet and mixed-wet conditions, while imaging the pore structures and the fluid invasion characteristics by laboratory-based X-ray micro-CT scanning. By performing the experiments quasi-statically, the quality of the micro-CT images is high enough to quantify microporosity and fluid saturations. Section 2 shows the experimental materials, procedures and data processing workflow. In section 3, we first introduce the observed pore filling behavior in the two samples under quasi-static flooding (section 3.1). The possible reasons leading to the gradually filling behavior in the mixed-wet sample are then analyzed based on the wettability characterization (section 3.2) and the analysis of the pore network characteristics (section 3.3). Section 3.4 provides a novel workflow to investigate the sensitivity of the multiphase flow properties to the slow movement of the fluid menisci, using a state-of-the-art multi-scale pore network model (PNM) for porous media with heterogeneous architecture and wettability distribution.

## 2 Materials and methods

### 2.1 Materials

There were two Luxembourg sandstone samples used in this study. The Luxembourg sandstone is a heterogeneous, calcareous quarried sandstone with complex pore structures, which consist of macropores and a significant fraction of microporosity (Molenaar, 1998). Mercury intrusion porosimetry on a sister sample showed it has a bimodal pore throat size distribution (supporting information Figure S1) centered on 2 µm and 20 µm and a porosity of 18.76% (Mascini et al., 2021). One sample was water-wet (WW) with 20 mm in length and 6 mm in diameter. Another (13 mm in length and 6 mm in diameter) was chemically treated to change the wettability by immersing the cleaned and dried sample in 25 ml of decane with 5 wt.% octadecyltrichlorosilane (OTS) for 24 hours, then cleaning the sample with isopropanol and drying. The treated sample was wrapped in teflon tape and stored in a desiccator. For more details on the wettability treatment, we refer to Mascini et al. (2021).

For the experiment, a brine solution made from deionized water doped with 25 wt% potassium

iodine (KI) was prepared as the aqueous phase to provide image contrast, so that the fluids in the pores could be distinguished. n-Decane was used as the oil phase.

### 2.2 Flow apparatus and procedure

The aim of the unsteady-state flow experiment performed here was to investigate the fluid invasion and distribution mechanisms during quasi-static oil and water flooding under different wettability conditions. Figure 1 shows the flow apparatus. The sample was placed in a fluoropolymer elastomer (Viton) sleeve with a hydrophobic and a hydrophilic porous plate fitted on its top and bottom, respectively. The tight pore sizes (150 nm in diameter) of the porous plates prevented the early breakthrough of invading fluid (i.e. hydrophobic and hydrophilic porous plates prevented brine and decane passing through at low pressures respectively) and created a relatively homogeneous saturation profile during fluid injection. The two end pieces connected the sample to the flow lines. This assembly was mounted in a PEEK hassler-type flow cell which is X-ray transparent (RS Systems, Norway). A Vindum Engineering VP-12 pump was used to pump the two fluid phases into the samples. The pressure drop over the sample was measured by a differential pressure transducer (Keller PD-33X).

The flow cell was mounted in the Environmental Micro-CT (EMCT) scanner at the center for X-ray tomography at Ghent University (UGCT) (Bultreys et al., 2016; Dierick et al., 2014). This is a gantry-based system with a rotating source-and-detector assembly. This ensured that the sample and flow lines were kept static during image acquisition. For the image acquisition, the X-ray tube settings were 110 kV and 8 W, the voxel size was 6.5 μm, and we used a 1.15 s integration time per radiograph for 2400 projections.

The experiment consisted of decane injection into a brine saturated sample, followed by brine injection. Both injections took place at low capillary numbers (Ca). The Ca is defined as the ratio of capillary forces to viscous forces ($Ca = \mu q/\sigma$, where $\mu$ is the dynamic viscosity of the injected fluid, $q$ is the Darcy velocity, $\sigma$ is interfacial tension between two fluids. Typically, the system is considered to be capillary dominated flow if Ca is lower than $10^{-6}$). For convenience, we will refer to the injection of decane and brine as oil and water flooding in following sections.

The confining pressures for both samples were kept at 3800 kPa during the whole process. After taking a dry micro-CT scan, brine was pumped into the samples for several hours, where the pressure drop over the samples was controlled at 3000 ± 100 kPa, to fully displace air inside, and a brine-saturated scan was taken when no more changes were observed in sample. Then, decane was injected slowly (capillary number $< 10^{-9}$) from top to bottom, while the bottom water-wet porous plate prevented the oil phase to pass through. For each sample, a set of controlled, increasing capillary pressure steps were imposed, each by adjusting the flow rate to obtain a constant low differential pressure over the sample and the capillary plates. For the water-wet case, we obtained 4 pressure steps at 2.5, 4, 6 and 27 kPa. For the mixed-wet sample, the capillary pressures were 2, 3.5, 4.5 and 6 kPa. Each pressure step was followed by a micro-CT scan after pumping 12 to 24 hours, when no changes were observed anymore on differential radiographs. Then, the flow was reversed: the decane pump was stopped, and brine was injected from the bottom to the top of the sample at 0.00008 ml/min for the water-wet sample and 0.0001 ml/min for the mixed-wet counterpart. Three micro-CT scans during this waterflooding process were taken for each sample, respectively. The top hydrophobic porous plate only allowed oil phase to flow out during this waterflooding process. Note that the reason we used a constant flow rate instead of constant pressure in this process is that for the water-wet sample, the invaded watery fluid always swells from micropores or smaller pores first. This can happen very quickly if the constant pressure is not controlled to a very high accuracy, resulting in fast oil phase trapping and reaching the residual oil saturation state in a short period of time. To avoid this risk, a very low constant flow rate was used in the waterflooding experiments on both samples. Considering that the imbibition in the water-wet sample can be expected to proceed faster than in the mixed-wet sample, we used a slightly lower flow rate for the former, to better record the fluid invasion process.

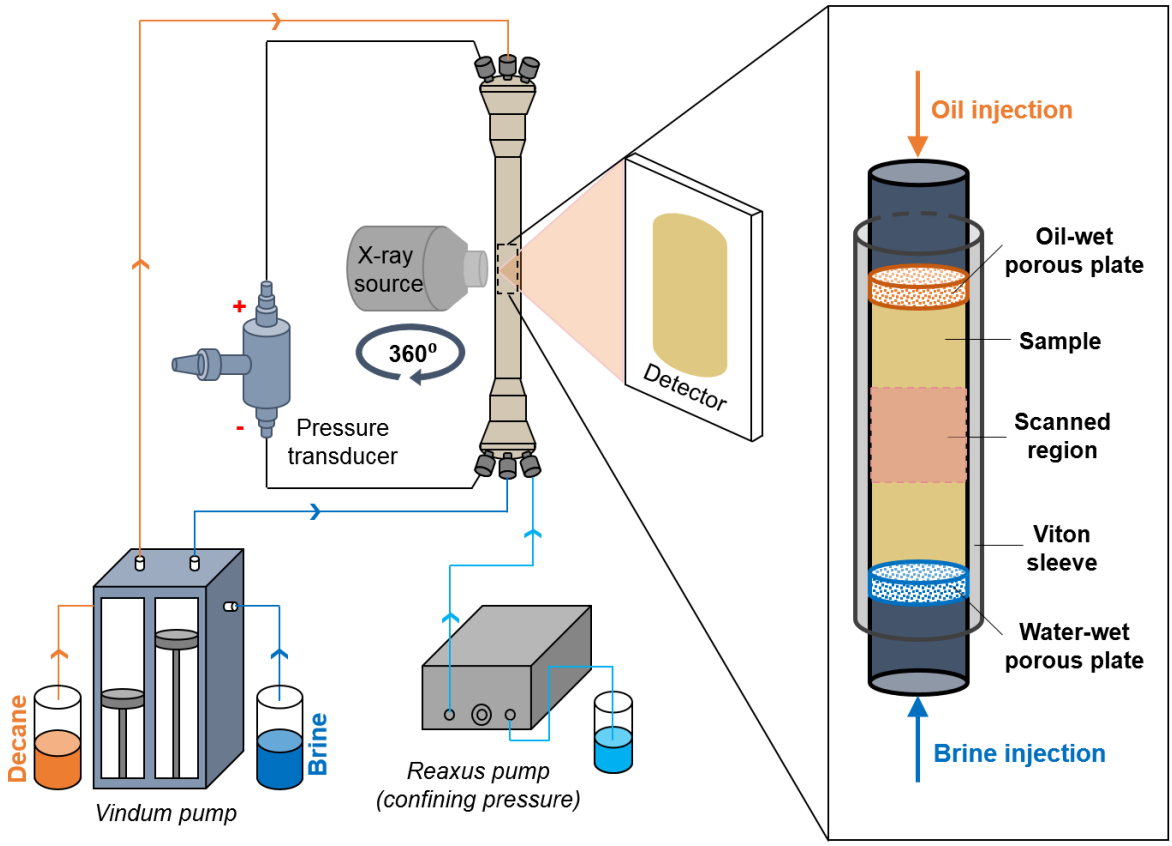


Figure 1. Experimental apparatus and detail of assembly inside the flow cell.

## 2.3 Image processing

After reconstruction, the Avizo 2020.2 (Thermo Fisher Scientific, France) software was used for image processing. All the images were registered using normalized mutual information to a reference scan and resampled with the Lanczos algorithm (Burger & Burge, 2010). This way, they were aligned in space. Following this, a non-local means edge-preserving filter (Buades et al., 2008) was applied to all images to reduce the noise. As can be seen in Figure 2, pore-filling and dissolution microporosity were commonly encountered. Because of the high X-ray attenuation coefficient of the KI in brine phase, the pores filled with brine had bright grey values in the images. In order to reduce segmentation errors, macropores were first segmented manually on the dry scan using histogram thresholding. The differential imaging method (subtracting dry scans from brine-saturated scans) (Lin et al., 2016; Wang et al., 2022) was used to identify microporous regions. Then, the rest of the voxels in the dry scan were assigned as solid grain phase. Figure 2 shows the three phase segmentation results. For multiphase scans,

the decane and brine within macropores were also classified with histogram thresholding, on which the labelled macro-pore space was used as a mask (Wang et al., 2022).

The porosity distribution can be calculated based on differential images between the brine saturated scan and the dry scan with the following equation:

$$\varphi_{micro} = \frac{I_{diff} - CT1}{CT2 - CT1} \quad (1)$$

where $I_{diff}$ is the grey value difference of two scans, *CT1* is the threshold value for solid phase (0% porosity), which was determined based on grey value at the boundary of the solid grain and microporous region in the histogram, *CT2* is the threshold value for macropores (100% porosity), which was obtained by masking segmented macropores on differential image and finding the peak value existed in the grey value histogram. Similarly, the saturation distribution map can also be obtained with multiphase-dry differential image. The full details are provided in our previous publication (Wang et al., 2022).

For curvature measurements, the marching cube algorithm was applied on the segmented waterflooding images to generate triangulated surfaces, which were smoothed by a Gaussian filter with a constrained smoothing extent of 3 voxels to remove noise and staircase-like artifacts (Li et al., 2018). Following this, the oil-brine surfaces were extracted and approximated locally by a quadratic form. The eigenvalues and eigenvectors, which represent the values and directions of two principal curvatures, of this quadratic form were used to calculate the mean curvature, i.e. $\kappa=(\kappa_1+\kappa_2)/2$. Due to the limited image resolution (6.5 μm) and the complex pore structures, the segmentation on the rough edges of oil-brine interface near solid materiel may generate unrealistic curvature values. We followed the procedures presented in (Mascini et al., 2020) and (Li et al., 2018) to filter data points. The curvatures which had a radius of curvature value smaller than twice the voxel size, i.e. $\kappa>1/(2*\text{voxel size})$, were first removed as they were likely affected by artifacts. Then, the geodesic distance of each triangle was calculated by averaging the three shortest vertex distances on it. The distance weighting combined with interface modification (25% of the maximum geodesic distance was set as the threshold to eliminate uncertainties caused by rough edges) method was used to

212 improve the curvature estimation by removing spurious values near the pore walls.

213 Wettability reflects the ability or tendency of one fluid to spread on the surface of a solid phase
214 when there are other immiscible fluids in the system. It is usually characterized by the contact
215 angle. In this work, an automated contact angle measurement algorithm (AlRatrout et al., 2018a)
216 was applied on segmented multiphase images to quantify geometric contact angle for both
217 samples.

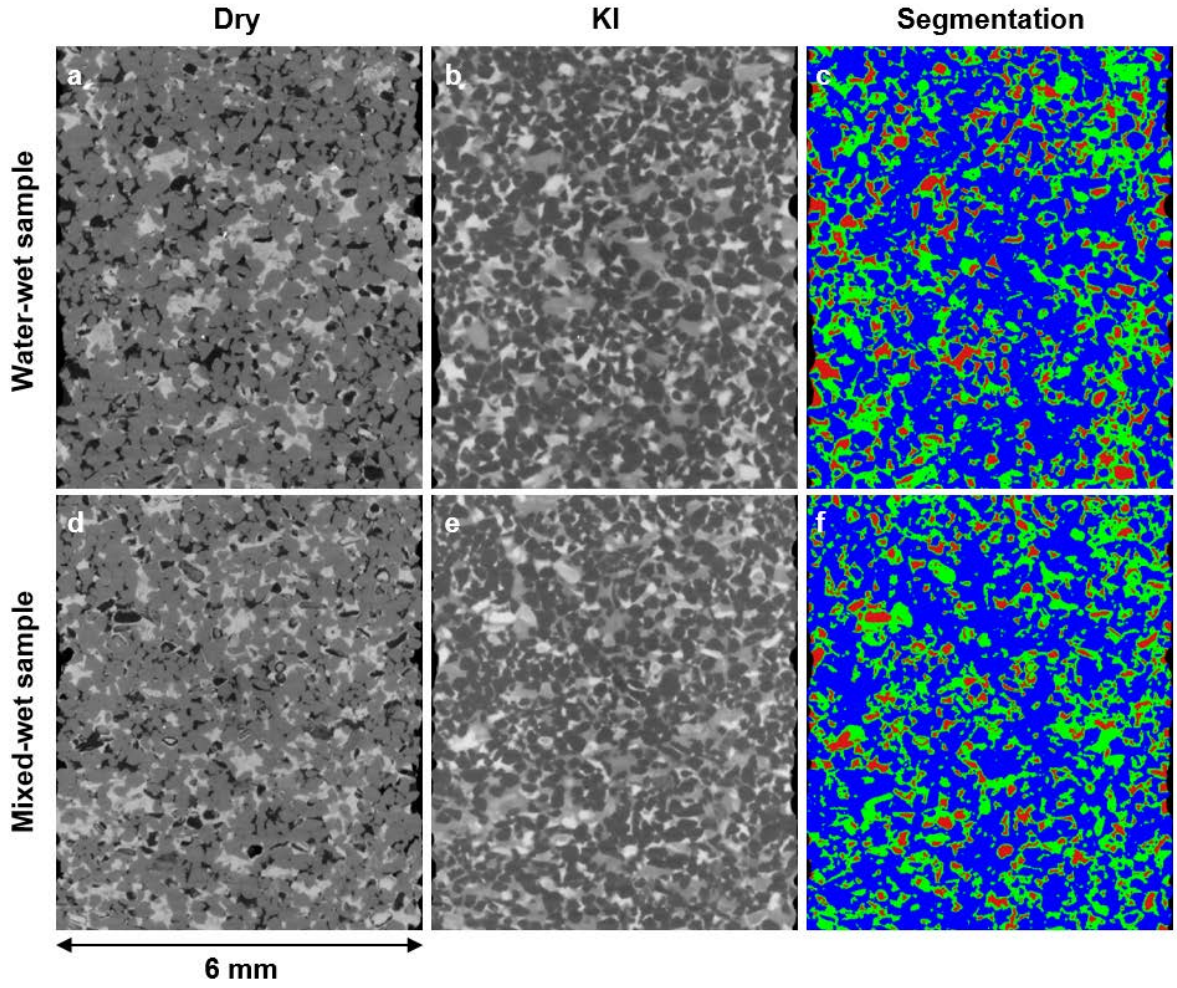


218

219 Figure 2. Two-dimensional cross-sections of filtered water-wet and mixed-wet samples. The top and bottom
220 rows show the dry scan, the brine-saturated scan and the three phase segmentation for water-wet and mixed-
221 wet cases respectively. The red, green and blue phases on segmentation map represent macropores,
222 micropores and solid grain.

## 3 Results and discussion

In the following, we first describe the fluid distributions and quasi-static filling processes observed in the pore space based on the micro-CT images. Then, the wetting state and the network characteristics were analyzed to understand the underlying mechanisms of the complex fluid invasion behavior. Finally, the simulations on multi-scale PNMs were performed to link the pore-scale displacement to the fluid flow properties.

### 3.1 Pore filling processes

The brine saturation profiles along flow direction in both macro- and microporous regions at each oil flooding pressure step are shown in Figure 3. For the water-wet case, the brine saturation dropped dramatically with pressure increase, presenting a relatively uniform distribution at the highest pressure. At this point, there was a high brine saturation (41.29%) in the micropores. This was 5 times as high as the brine saturation in the macropores at the end of oil flooding. Under mixed-wet condition, the brine saturation in the micropores was also higher than in the macropores at all pressure steps, but the difference was smaller. This indicates weakly water-wet conditions in the microporosity.

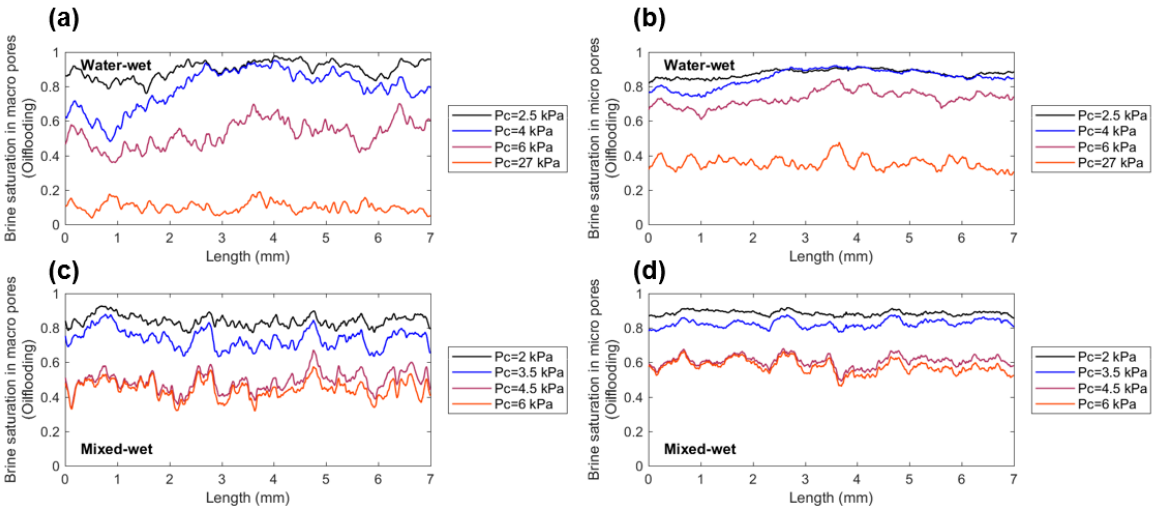


Figure 3. Average brine saturation distribution during the oil flooding, in slices perpendicular to the flow direction within macropores (left) and micropores (right) for water-wet and mixed-wet samples.

Figure 4 shows the evolution of the brine and oil clusters in macropores of the water-wet sample.

During the oil invasion sequence (Figure 4(a)), the oil found a main flow path and formed several large clusters in the macro-pore space first, followed by occupying more and more pores, while the brine phase gradually appeared more isolated. For a water-wet porous medium, the typical displacement mechanism during oil flooding is a series of Haines jumps (Burst flow) (Berg et al., 2013; Bultreys et al., 2015), i.e. a sudden rapid fluid interface movement through a local constriction in the pore space, due to the dependence of the equilibrium capillary pressure on the channel radius. As we aim to study the fluid distribution after a period of equilibration at certain set capillary pressures, the images only reflect the fluid filling state after many of these events. The branched structure connecting large pores together is consistent with a capillary fingering type fluid distribution pattern that results from successive Haines jumps (Blunt et al., 1992; Herring et al., 2014).

In the water-wet sample the waterflooding that followed the oilflooding increased the brine saturation in the macroporous region from 8.5% to 22.7%, compared to that in the micropores increasing from 50.7% to 79.3%. It is clear that in the resolved pore space (Figure 4(b)), brine preferentially entered pores or throats with smaller sizes. In this process, brine films residing in the corner or crevices of pores/throats at the end of oilflooding started to swell with the decrease of capillary pressure, causing the interface configuration to become unstable when films on opposing sides of the pore surface touched each other. On the micro-CT images, we could clearly see a large amount of trapping due to snap-off, such as the example shown in Figure 5.

For the mixed-wet case, on the other hand, the brine was displaced even at low pressures during oil flooding. More small-volume brine clusters resided in the pore space, keeping the brine connected, see Figure 6(a). The oil injection in the resolved pores of the mixed-wet sample was different from the water-wet case: it tended to enter oil-wet or weakly water-wet pores at the beginning of the displacement rather than filling the pores in order of their size (Scanziani et al., 2020). The oil cluster volume distribution was therefore much smaller than in its water-wet counterpart: e.g. the largest oil cluster volume at 6 kPa was 14% of the macropore volume for water-wet (7.32 $mm^3$) and 2% of the macropore volume (0.59 $mm^3$) for mixed-wet. During

waterflooding of the mixed-wet sample, the brine saturation increased by only 3% in macropores, and brine and oil cluster size distribution did not change significantly (Figure 6(b)). While that in micropores showed a 5% increase. Compared to a sudden increase of brine saturation in micropores of water-wet sample when the waterflooding started, that change in micropores of mixed-wet case was much lower.

In comparison with the conventional pore filling phenomena for water-wet conditions, the fluid flow mechanisms in the mixed-wet sample appeared to be more complex (Figure 7). The micro-CT images showed that the fluid occupancy of most macropores made a step change from a certain pressure step to the next. However, “gradually filling” events described by Mascini et al. (2021) were also observed. This manifested itself in pores where terminal menisci appeared to be quasi-stable everywhere while the three-phase contact line passed through it. Each such pore was thus only partially invaded in between consecutive pressure steps. The menisci in such pores remained present for multiple pressure steps at intervals of more than either 12 or 6 hours (respectively for oilflooding and waterflooding). The menisci curvatures gradually increased or decreased with the imposed capillary pressure, reflecting the local capillary pressure change. By detecting the interface movement at each pressure step during the experiment, 3.4% of the macropores in oilflooding and 2.8% of the macropores in waterflooding were found to reflect “gradually filling” phenomena, where these pores accounted for 13% of the macropore volume. For convenience, we will refer to these as “gradually filling pores” and to the others as “capillary instability pores” in the following sections.

The morphology of the fluid menisci in gradually filling pores was markedly different from the water-wet case, leading to three observations. The first observation is that the invading and retreating of fluid in some pores can be approximated as a reversible process. As shown in pore A (Figure 7(a)), the invading meniscus changed from a convex to a flat interface during oil injection, and then bulged into oil again with the decrease of pressure, during which the negative principal curvatures dominated over positive principal curvatures. The second observation is a near flat front at the end of each oil flooding step in several pores (as shown in

298 Figure 7(b)), indicating intermediate-wet conditions. The third observation is that the oil
299 flooding behavior in certain pores (Figure 7(c)) were distinct from that seen in the water-wet
300 case, where the large pores and throat were preferentially invaded by the oil phase, followed
301 by those with smaller sizes and finally microporosity, as these had high capillary invasion
302 pressures. To investigate this, we divided the microporosity near pore C in Figure 7(c) into 2
303 regions and tracked their grey value change. This showed that there was a significant decrease
304 of brine saturation in microporous region 2 compared to that in the microporous region 1.
305 Furthermore, the brine was completely displaced out of pore C while its saturation in
306 microporous region 1 was still high. This is likely due to the effect of wettability, which
307 impacted the order of filling here. This hypothesis will be further analyzed in the next section.

308 Overall, this section clearly shows that the fluid displacement behavior in both the 3D network
309 and in a single pore are markedly different in the untreated and treated rock samples. Further
310 analysis on wettability distribution and the neighboring network characteristics of pores in
311 treated sample will be presented in the following sections to point out the possible causes.

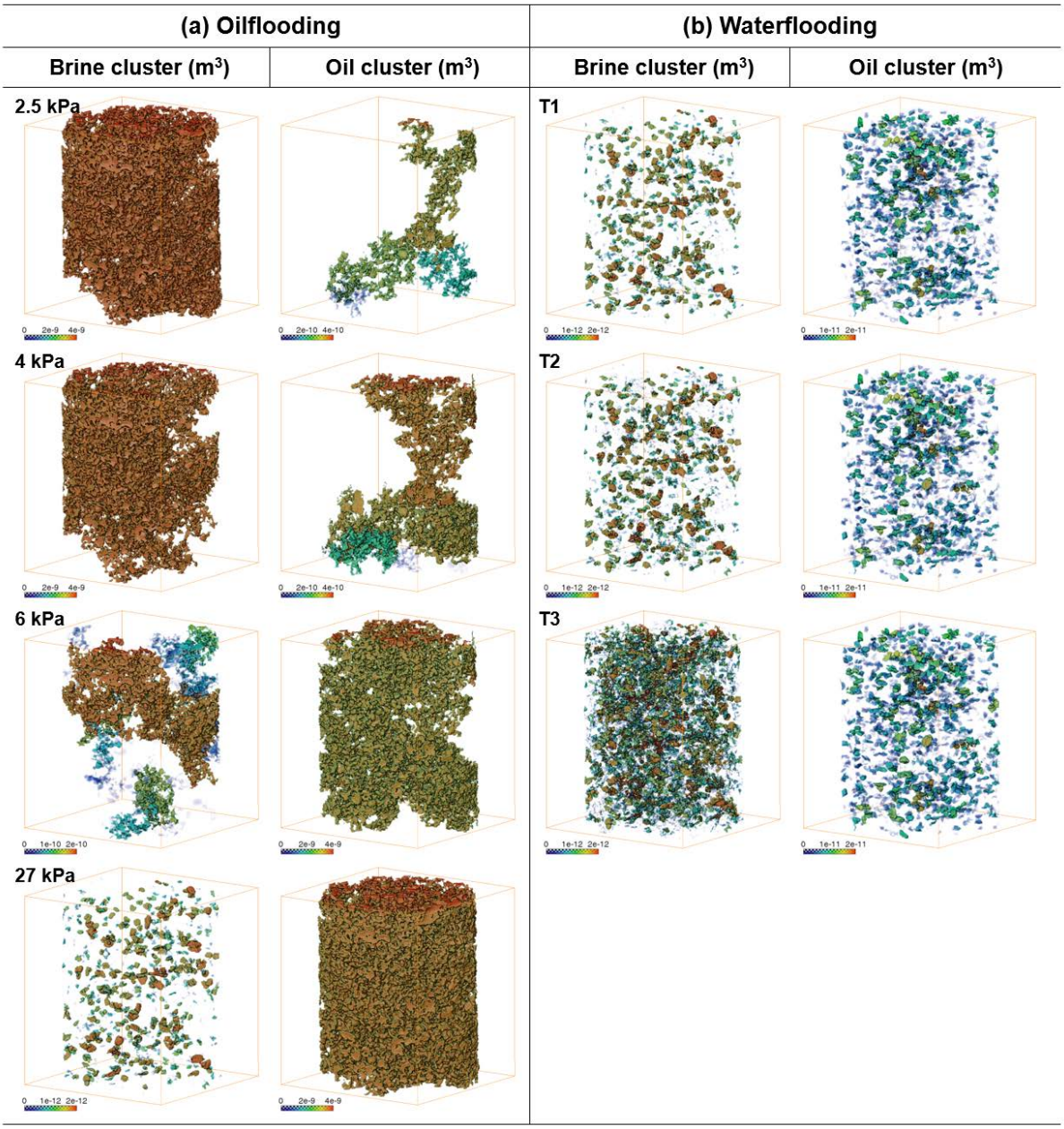


312

313 Figure 4. Fluid cluster changes in macropores of the water-wet sample during (a) oilflooding and (b)

314 waterflooding. The color shows cluster volume ($m^3$).

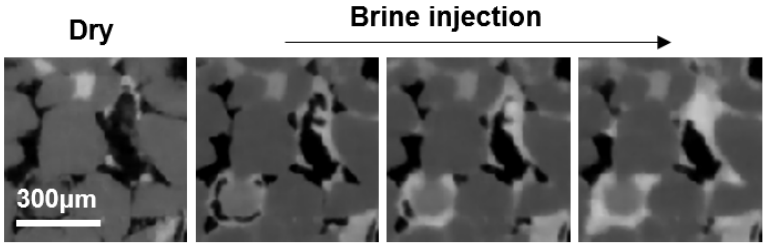


315

316 Figure 5. Example of two-dimensional views of oil phase trapping in pores under water-wet condition.

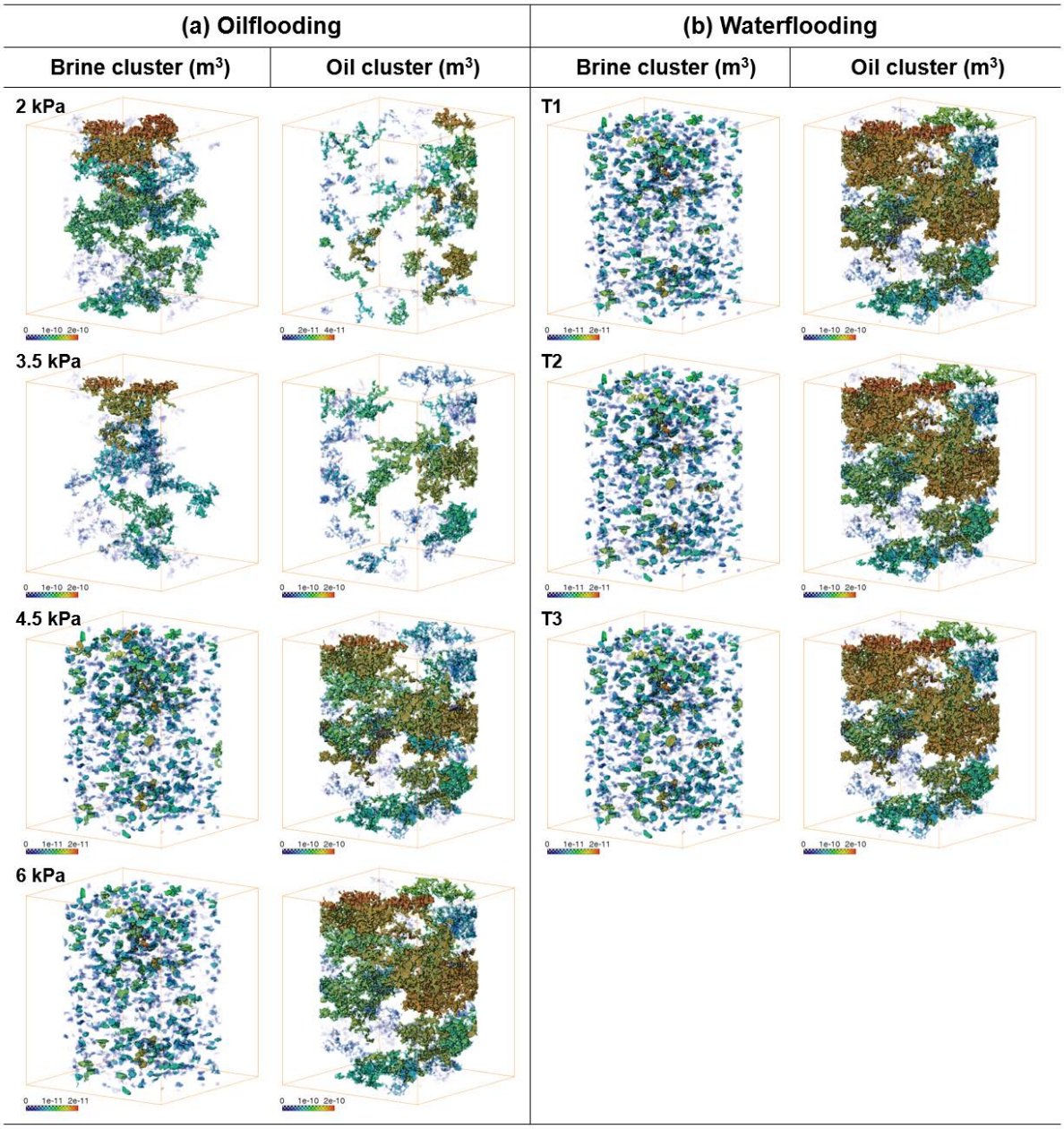


Figure 6. Fluid cluster changes in macropores of the mixed-wet sample during (a) oilflooding and (b) waterflooding. The color shows cluster volume ($m^3$).

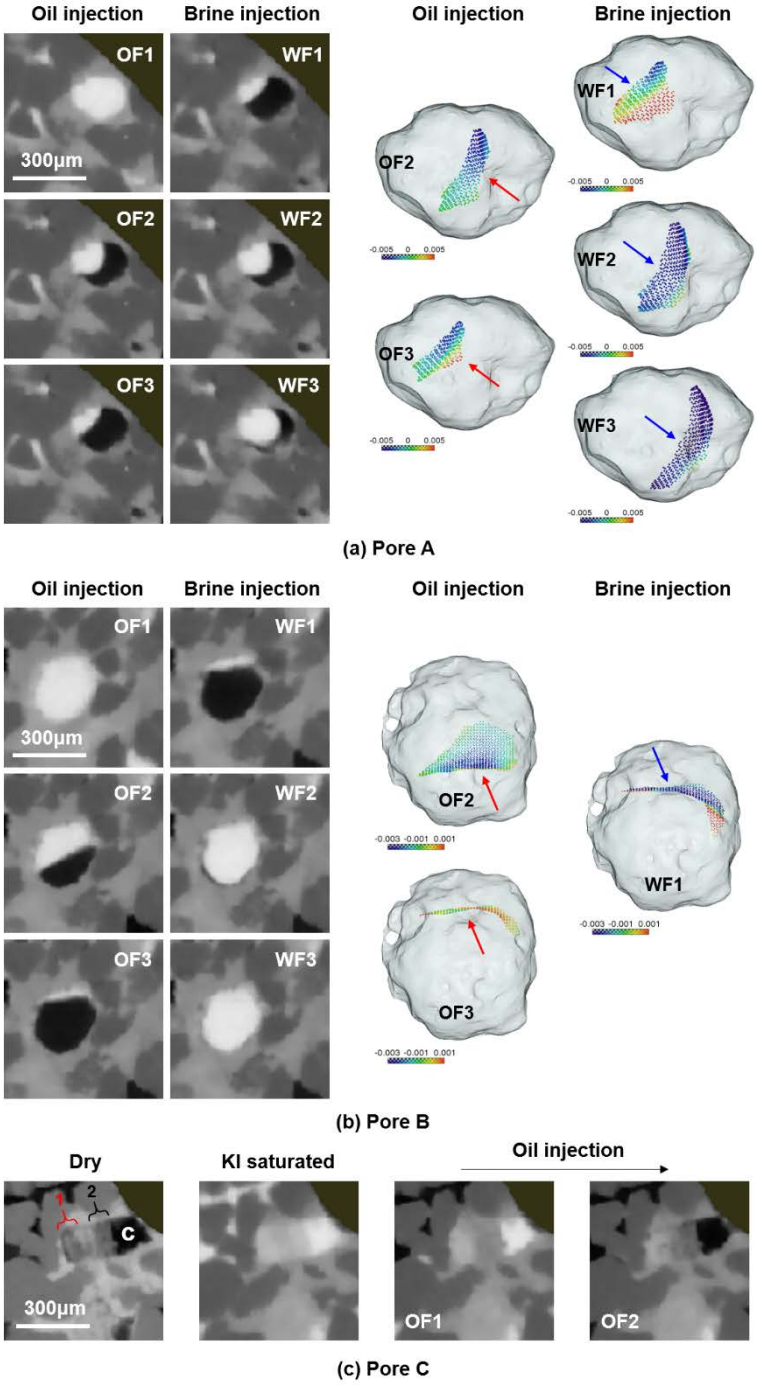


Figure 7. Examples of fluid invasion in pores of mixed-wet sample. (a) Oil-brine interfaces variation during oil and subsequent waterflooding in pore A. The figures on the left are 2D slices on X-Y plane. The figures on the right indicate the interfaces movement and the mean curvature distribution (colorful dots on interfaces) in 3D transparent pore space. The red and blue arrows show invasion direction of oil and brine phases respectively. (b) Movement of a flat shape interface on a 2D slice of pore B in oilflooding and waterflooding. (c) Invasion of oil phase from microporous region to a macropore C in oilflooding. The microporous phase

is divided into 2 regions according to their grey value change in oilflooding process.

### 3.2 Wettability characterization

For the resolved macropores, the wettability can be quantified by measuring the contact angle. Figure (8) shows the results of geometric contact angles that were measured on full, segmented micro-CT images at the last waterflooding step. The untreated and treated samples had a mean contact angle of 69.23° and 95.50° respectively. The treated sample had a contact angle distribution with a very broad range of values above and below 90°, implying a mixed-wet state, while the contact angle distribution of the untreated sample implied weakly water-wet conditions. Because the contact angle was calculated based on three-phase contact lines extracted from the micro-CT images, the image resolution, selection of filtering methods and segmentations affected measurements. In addition, the roughness of the pore surfaces in these samples may also have been a key factor leading to wide range of contact angle, due to contact angle pinning and hinging that is not picked up in static measurements (AlRatrout et al., 2017). To investigate the wettability in gradually filling pore, Figure 8(b) presents the contact angle distribution on pore A and pore B (micro-CT images are shown in Figure 7(a)) extracted from the mixed-wet sample. Typically, the fluid meniscus remains concave (oil bulging into brine) in water-wet pores, and is convex (brine bulging into oil) in oil-wet pores. However, the wettability of the pore surfaces shown here was very heterogeneous, appearing to be partially water-wet and partially oil-wet. The complex interaction between contact angle and pore space geometry led to a variation in the interface morphology, resulting in both negative (i.e. oil bulging into brine direction) and positive (i.e. brine bulging into oil direction) mean interfacial curvatures occurring on the same fluid meniscus (see colored dots shown in 3D pores in Figure 7). Therefore, the movement of the invading phase in these mixed-wet pores might be inhibited temporarily, but facilitated at the next time step, resulting in complex invasion behavior in the pore space.

For the unresolved micropores, it is impossible to measure the contact angles directly, because the fluid interfaces are not resolved. We therefore estimated the wetting state of the

354 microporosity by quantifying the evolution of its saturation based on the saturation maps from
355 differential imaging. Figure 8(b) shows an example of the application of this method on
356 microporous regions (the division of each region is shown in Figure 7 (c)) near pore C. The
357 decrease of brine saturation at each pressure step in the microporous regions of the water-wet
358 sample were very small, indicating that they were strongly water-wet: in this case, the filling
359 follows the order of pore size. However, the wettability of the microporosity in the mixed-wet
360 sample was more complicated, and it proved difficult to define a single wetting state obtained
361 from an average result to describe its characteristics. In the microporous regions that neighbour
362 pore C shown in Figure 7 (c), the saturation in region 2 decreased strongly, while that in region
363 1 was comparable to the average value of the whole microporous phase. Considering that the
364 saturation in pore C decreased to 0 already at a lower pressure (4.5 kPa), pore C is expected to
365 be more hydrophobic that microporous region 1. Therefore, we estimate that the latter is weakly
366 water-wet or weakly oil-wet and that microporous region 2 is strongly oil-wet. This means the
367 pore size was likely not the dominating factor for the filling sequence in the mixed-wet sample.

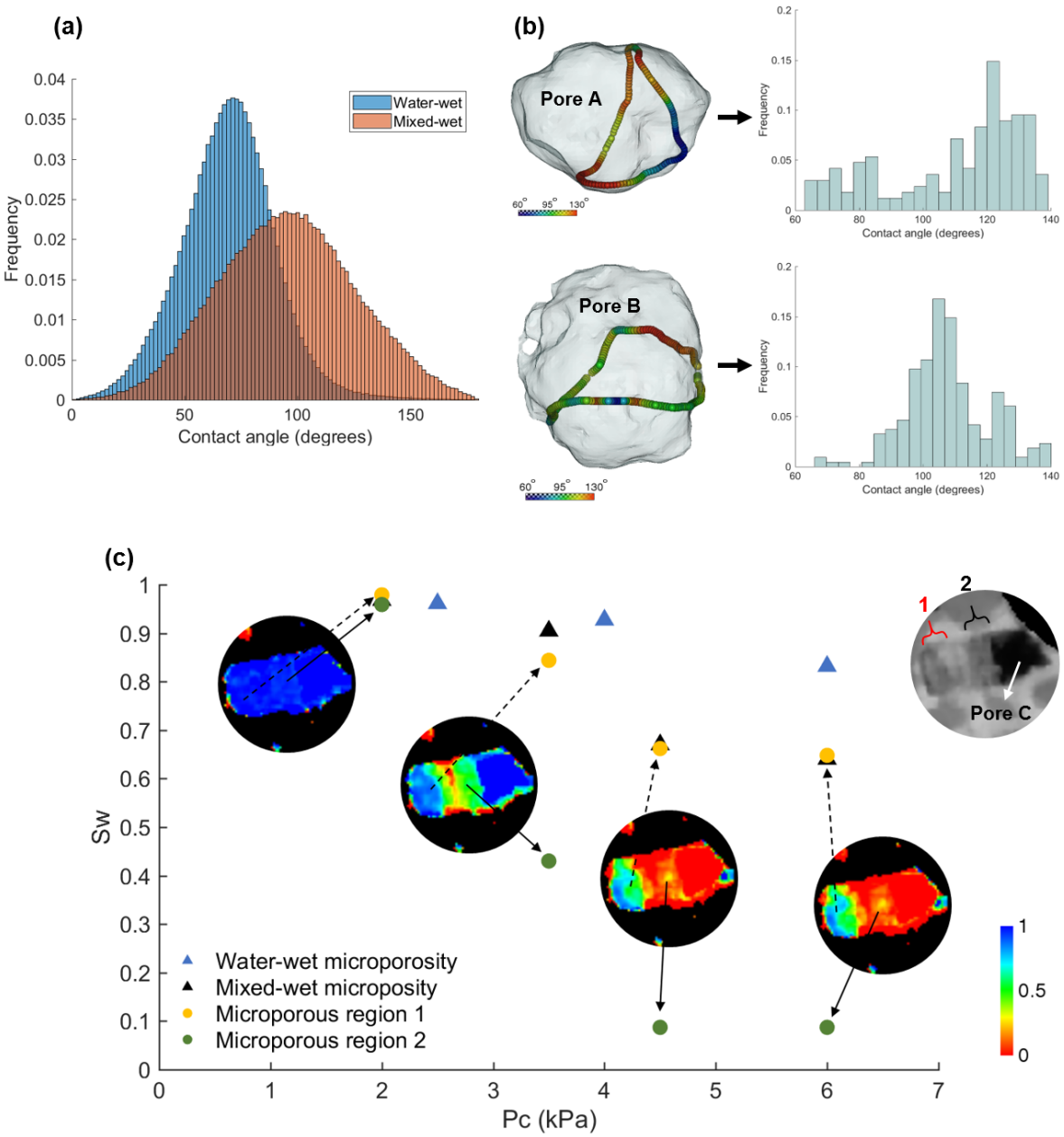


Figure 8. (a) Histogram of geometric contact angles measured on images after waterflooding under both conditions. (b) Example of contact angle distribution on pore A (top) and pore B (bottom) under mixed-wet condition and the corresponding distribution histograms. (c) Estimation of the wettability of the microporosity based on saturation change. Note that the saturation mentioned here is the average brine saturation in the microporous phase of the whole sample (triangle symbol) and in the specific microporous regions (circular symbol) in the oilflooding process. The four circular images show the saturation distribution map in microporous region 1, microporous region 2 and pore C at different pressure steps.

### 3.3 Pore network characteristics

#### 3.3.1 Multi-scale pore network extraction

Extracting PNM from micro-CT images is an important tool to better understand the characteristics of the pore space (Bultreys et al., 2015). The goal is to simplify some of the network's complexity while its salient characteristics such as topology and geometry are preserved. Because the samples used in this study presented multi-scale features with both resolved macropores and unresolved micropores (i.e. pores below image resolution), and the microporosity can play a key role in making the fluid flow behavior complex as stated in previous section for the mixed-wet case, a state-of-the-art of the multi-scale modelling technique (Ruspini et al., 2021) was used here. While direct multi-scale simulators are being developed (Soulaine et al., 2016; Zhang et al., 2016), multi-scale PNM are currently still one of the only models that allow to incorporate the microporosity characteristics on fairly large image sizes for this type of complex samples. The extraction algorithm simplified the pore geometry into 4 types of network elements: pore bodies and pore throats representing local dilations and constrictions in the macroporous space, and Darcy nodes and links corresponding to the (unresolved) microporosity phase treated as a continuum porous medium. The model was constructed based on a 3D porosity map and a 3D rock type map (i.e. different flow zones for the unresolved regions). Individual pore networks for the resolved pores and each of the rock types were extracted first and then merged into a single multi-scale PNM by creating a virtual link in the contact area between pores from different, neighboring zones. The porosity map was used to determine the local porosity in each element, and each flow zone on the rock type map was assigned different multiphase flow properties in the simulation process (the details will be described in the next section).

The porosity distribution information is shown in Figure 9(a) and Table 1. The total porosity was 18.11% and 15.14% for the water-wet and mixed-wet cases respectively. More than 30% of the samples' volume fractions were made up of microporous voxels in both cases, and their contribution to total porosity was equally important as the macropores. Therefore, the presence

of microporosity increases the complexity of the pore space architecture, which may play an important role in the multiphase flow. For the determination of the rock type map, we introduced a method based on micro-CT images of obtained during capillary pressure experiments in (Wang et al., 2022). The method was validated to be a promising approach in decreasing the uncertainty of modelling, and was therefore used here. In this method, the saturation and the corresponding capillary pressure of each microporous voxel in the sequence of experimental images were first fitted using a Brooks-Corey-type Pc formulation (Brooks & Corey, 1966) to obtain the invasion-capillary-pressure (Pct) distribution map of the sample. Then, thresholds determined by k-means clustering were applied on the Pct map to divide the microporous region into 3 rock types for both samples, see Figure 9(b).

It should be noted that in this study, the goal was to use the multi-scale PNM method to understand the connectivity structure of the sample, and to try to estimate how it may influence the flow behavior, rather than using it as a predictive simulation tool which aims to perfectly match the experiments or predict properties.

### 3.3.2 Network characteristics around gradually filling pores

The properties of the two extracted PNMs are shown in Table 2. According to the network model of the mixed-wet sample, we obtained the coordination number (CN) of 77, 139 and 90 for pore A, pore B and pore C respectively (micro-CT images are presented in Figure 7). The CN reflects the amount of neighbours each pore has. The CN of pore B only consisted of Darcy links, which means pore B was disconnected from all resolved pores and only connected by unresolved pores. The average microporosity around pore B was 0.46. For pore A and pore C, more than 97% of the CN were Darcy links (i.e. only 2 resolved throats around pore A and 3 resolved throats around pore C) with average microporosity of 0.46 and 0.57 respectively. Especially in pore C, the average aspect ratio (the ratio of pore body size to pore throat size) of the resolved throat configuration was very high (4.59). This likely explains the two crucial roles of microporosity in gradually filling event: (i) slowing down the pore-scale invasion, (ii) maintaining the connectivity of multiphase flow through complicated pore space, especially in

the isolated macropores. This may also be a possible reason why this invasion process was not reported in other relatively homogeneous mixed-wet media (Scanziani et al., 2020).

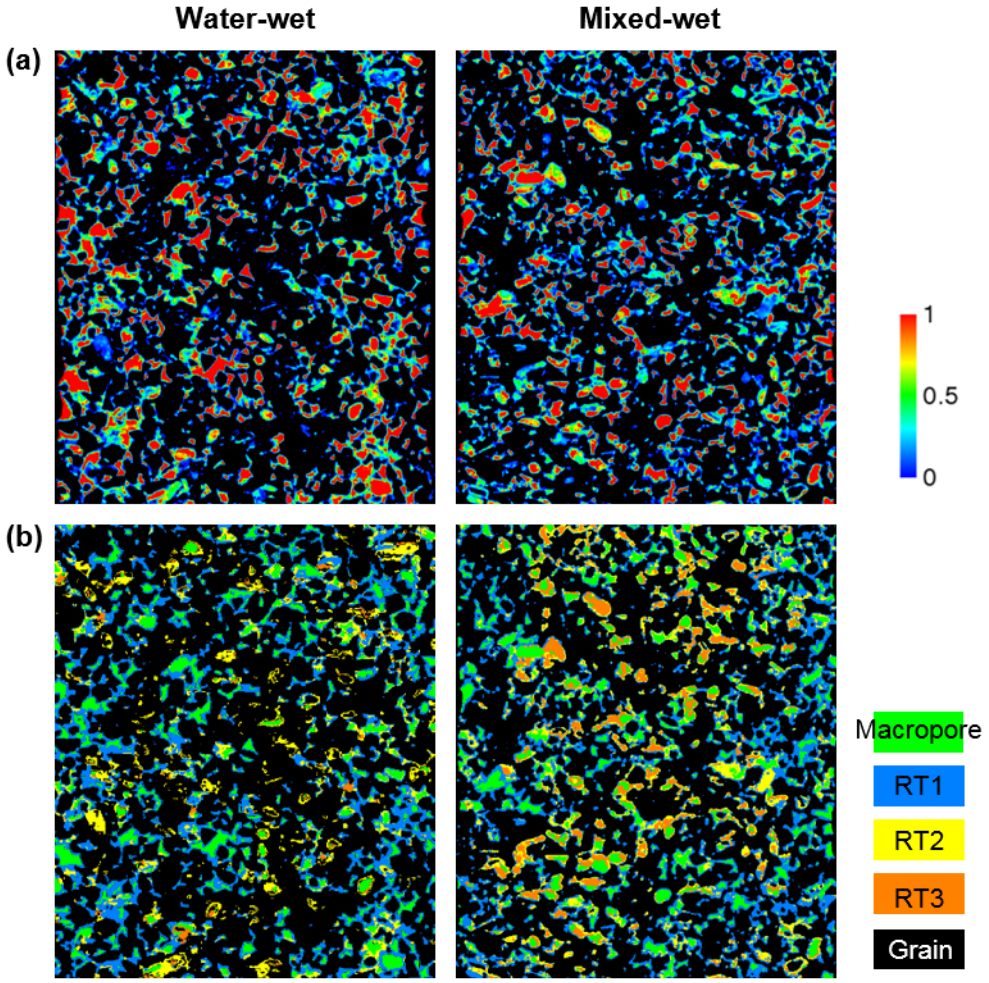


Figure 9. (a) Porosity distribution maps for water-wet (left) and mixed-wet samples (right). (b) Rock type maps for water-wet (left) and mixed-wet samples (right). On the rock type maps, the macropore region and solid grain are shown in green color and black color respectively. The RT1, RT2 and RT3 refer to 3 microporous regions with invasion capillary pressures from low to high values.

Table 1 Porosity and volume fraction of each phase in the samples.

| Sample | Phase | Average porosity | Volume fraction | Contribution | Total porosity |
|---|---|---|---|---|---|
| Water-wet | Macropore | 1 | 0.0954 | 0.0954 | 0.1811 |
| | Micropore | 0.2756 | 0.3109 | 0.0857 | |
| | Solid grain | 0 | 0.5937 | 0 | |

| | | | | | |
|---|---|---|---|---|---|
| | Macropore | 1 | 0.0741 | 0.0741 | |
| Mixed-wet | Micropore | 0.2554 | 0.3027 | 0.0773 | 0.1514 |
| | Solid grain | 0 | 0.6232 | 0 | |

Table 2 Properties of the multi-scale PNMs for two samples.

| Properties | Water-wet | Mixed-wet |
|---|---|---|
| Resolved Nodes | 53393 | 57468 |
| Resolved Links | 32372 | 20606 |
| Darcy Nodes | 427392 | 526917 |
| Darcy Links | 2352556 | 2902592 |
| Average CN (Resolved Nodes) | 12.15 | 11.76 |
| Average CN (Darcy Nodes) | 9.63 | 9.80 |
| Average macropore radius (μm) | 15.13 | 12 |

### 3.4 Influence of gradually filling event on flow properties

Quasi-static PNM (such as the one used here) by definition do not allow to simulate the dynamics of multiphase flow, for example the slow movement of the fluid menisci in the pores. These models assume that the capillary forces play a dominant role in controlling the invasion order of fluids in the pore space, so that the macropores change fluid occupancy in a single pressure or saturation step, while the influence of viscous forces on the displacement sequence are entirely neglected. Dynamic models, on the other hand, are computationally much more complex, and are therefore difficult to use in the complex samples investigated here. To nevertheless study the sensitivity of flow properties to gradually filling pores, we established two quasi-static models with different network structures for the mixed-wet sample. Model A was already introduced in section 3.3.1; this was a conventional multi-scale PNM without considering “gradually filling” behavior in certain macropores. It included 1 macropore phase, 3 types of microporous flow zones and 1 solid grain phase. In model B, gradually filling macropores were treated as “microporosity”: we applied the aforementioned “rock typing” method on them to divide a single macropore into different flow zones (Figure 10). It should

be noted that the goal was to make the effective behavior of the quasi-static PNM similar to the experiment without including the detailed physics of the process. To differentiate the fluid invasion mechanism in microporosity and in gradually filling macropores in the model, the properties for gradually filling regions were user-defined so as to obtain a gradual filling here. The model can only be expected to give a coarse estimate of what the inclusion of this behavior on the simulation would be, rather than provide accurate ab-initio prediction results. As shown in Figure 10(c), each flow zone was assigned an invasion capillary pressure according to the segmentation thresholds, which means the zone would be invaded by oil phase when the injection pressure reached this pressure. This way, we simulated the effect of the "gradual filling" process in macropores. This model contains 1 macropore phase, 3 microporous flow zones, 3 gradually filling zones and 1 solid grain phase.

The input petrophysical properties for each rock type included capillary pressure curve (Pc-curve), relative permeability (kr-curve) and permeability. The input Pc-curve was completely based on our experimental data (for more details regarding this procedure, we refer to our previous publication (Wang et al., 2022)). The kr-curve was obtained based on the Brooks-Corey model. A power correlation $k = a \cdot \varphi^b$ was used to determine the permeability for each node in the model, where we fixed the parameter *b* and tuned the parameter *a* until the output Pc-curve matched the experimental data (Ruspini et al., 2021). A Gaussian distribution of contact angles were assigned with values between $10^{\circ}$ and $160^{\circ}$ to mimic the complex wetting state of the sample. All the aforementioned parameters were the same for two models, except that in model B, the permeability of the gradually filling pores was assigned from a very small value (i.e. case 1 in Figure 11(a)) to a very large value (i.e. case 2 in Figure 11(a)). This is meant to perform a sensitivity study on the importance of these pores on the flow, by mimicking that these pores are open for flow or that their contribution to the flow is negligible. In this test, we only simulated the oil flooding process.

The results showed that the absolute permeability of model A was 29.86 mD. For model B, as shown in Figure 11(a), the absolute permeability of the sample remained approximately stable when the permeability of gradually filling pores was set lower than 1 mD or higher than 100

D, presenting an S-shape in the semilog coordinates. The total effect of gradually filling pores on the permeability of the sample was therefore 6 mD, approximately 19% of the maximum value. Figure 12 shows the comparison of the Pc-curves and the kr-curves simulated by different models. All Pc-curves had a good match with the experimental data and there is very little difference between the two models. The former was due to the fact that the input Pc-curve for Darcy pores were scaled with their porosity and permeability. The kr-curves indicated that gradually filling pores may affect the relative permeability of the brine phase, but that their effect is small. As depicted in Figure 11(b) and (c), the gradually filling pores were surrounded by micropores, which provided their connection with the other macropores and throats. During the oil flooding process, the case where the gradually filling pores had very low permeability (case 1) simulated that these pores were fully occupied by brine and the oil could not enter. This provided more flow paths for the brine, thus the brine relative permeability was higher. If their permeability was very high (case 2), the invading oil would pass through these pores easily, causing the brine to lose connected pathways, causing the brine relative permeability curve to decrease. As the model used in this study did not take into account the rate effects on the relative permeability, further developments in dynamic simulations are needed to fully investigate the results presented here.

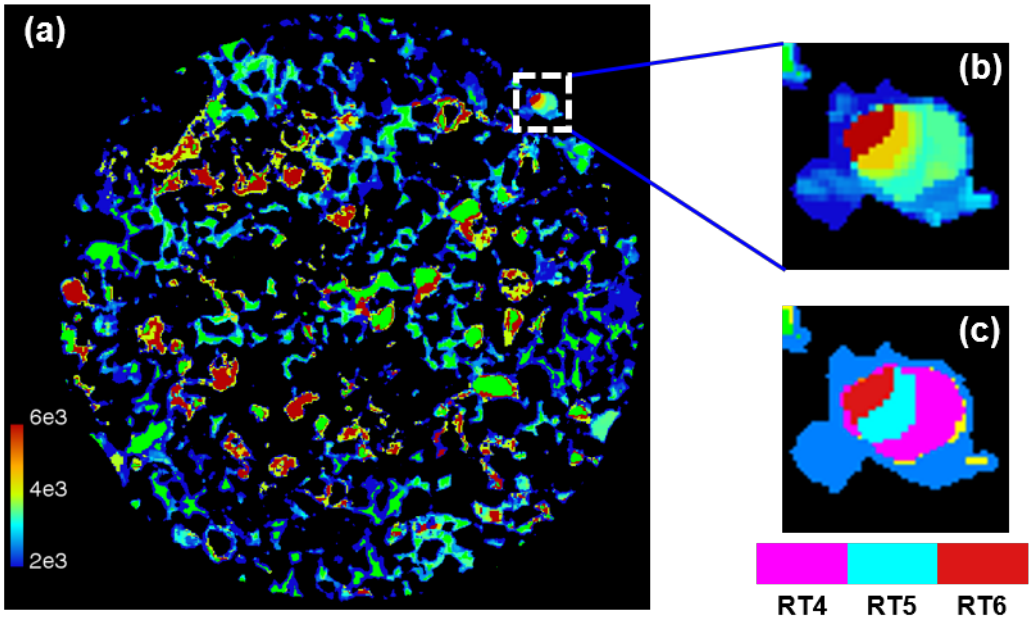


Figure 10. (a) A slice of invasion capillary pressure distribution on X-Y plane of the mixed-wet sample. The

501 "capillary instability pores" are marked in green. (b) A zoom in view of "pressure distribution" in pore A.
502 Note that the pressure in "gradually filling pores" does not have the same meaning as in the microporosity.
503 It only represents the moving sequence of fluid-fluid interfaces in macropores, i.e. "low pressure region" is
504 invaded first, followed by the "high pressure region". (c) An example of "rock typing" results for pore A in
505 model B. The segmentation of RT1-RT3 in model B is the same as model A, see Figure 9b. The RT4, RT5
506 and RT6 represent gradually filling zones.

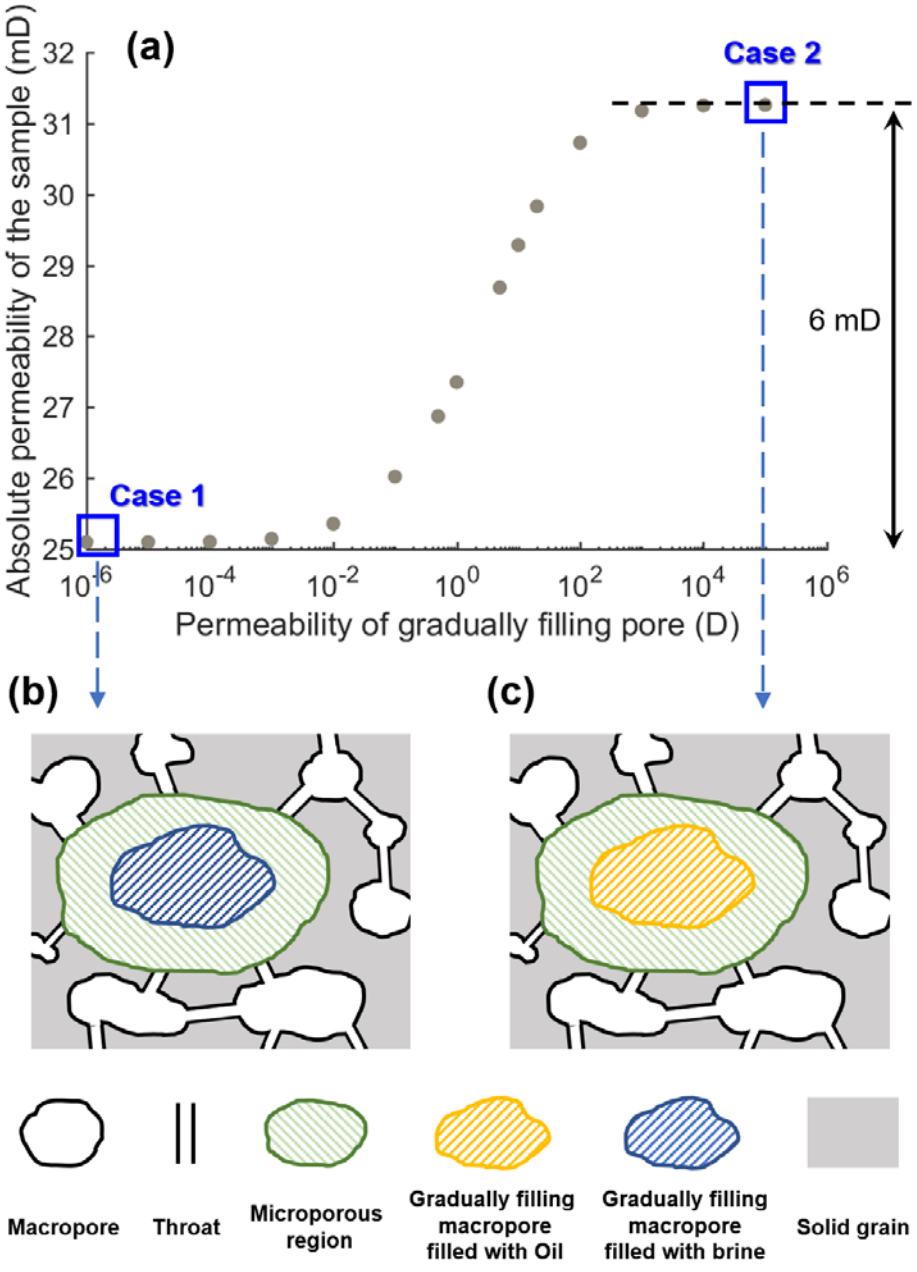


507

508 Figure 11. (a) Simulation results of the input permeability value for gradually filling pores and the absolute
509 permeability of the sample. (b) Diagram of the gradually filling pore blocked by brine at very low

permeability condition during two phase flow. (c) Diagram of the gradually filling pore blocked by oil at very high permeability condition during two phase flow.

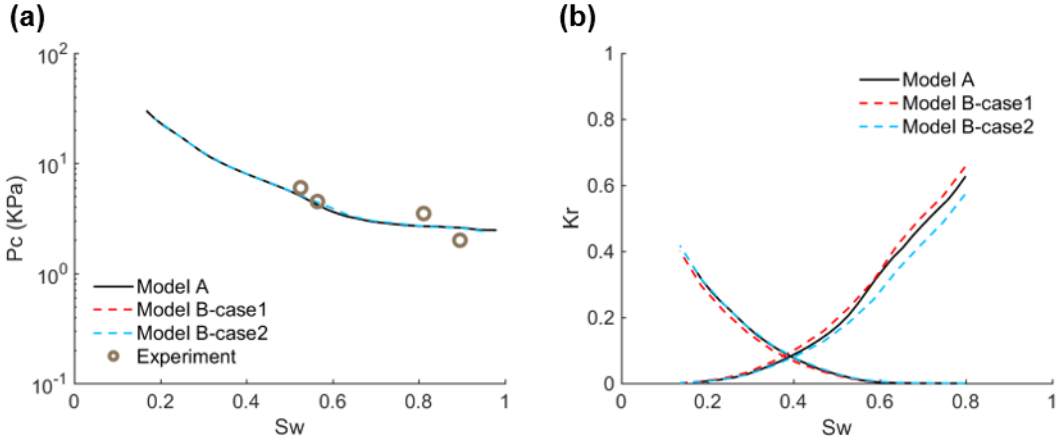


Figure 12. Results of oilflooding simulations. (a) Comparison of capillary pressure curves from the two models and the experiment. (b) Relative permeability curves of the two models.

## 4 Conclusions

We present an experimental workflow based on X-ray micro-CT to study fluid invasion behavior in heterogeneous rocks with different wettability via quasi-static oil- and waterflooding. We observed typical oil phase trapping in macropores of a water-wet sample during waterflooding, while in its mixed-wet counterpart, some macropores were observed to be filled gradually compared to others that were completely occupied by invasion fluid in a single pressure step. This occurred during both oil flooding and water flooding. To understand why and how the gradually filling pores behave under mixed-wet conditions, we analyzed the wettability and pore network characteristics. We introduced a new approach to perform a sensitivity study of the impact of the slow displacements on the multiphase flow properties, using a state-of-the-art multi-scale PNM.

We quantified the wettability of macropores in each sample by measuring the contact angle on multiphase micro-CT images, and found that the gradually filling pores in mixed-wet case had a high degree of wetting heterogeneity on their pore walls, presenting partially water-wet and partially oil-wet regions. This may alternately inhibit and facilitate the movement of invading

phase at different times during displacement, resulting in complex invasion behavior in the pore space. In this study, the wettability of the microporosity was evaluated by quantifying its saturation, shedding new light on the slow displacements first characterized by Mascini et al. (2021). The results indicated that the mixed wettability impacted the pore filling sequence and increased the complexity of multiphase flow. To mimic the slow movement of menisci in the model and the importance of this factor in flow simulation, we constructed two multi-scale PNMs. One was a conventional model with macropore phase, solid grain phase and 3 microporous flow zones classified by fitting saturation and capillary pressure of each voxel. It showed that the gradually filling pores presented a high CN, and more than 97% of the CN was contributed by micro-elements. This proved that the microporosity provided the “supply chain” for the gradually filling pores, which on one hand slowed down the pore-scale invasion and on the other hand maintained the connectivity of fluids in those macropores. The second model had the same segmentation of “capillary instability pores”, microporous phase and solid grain as the previous model, except that the gradually filling macropores were divided into distinct invasion zones to mimic their slow filling. The results showed that the total effect of gradually filling pores on the permeability of the sample was 6 mD (approximately 19% of the maximum value), but that their influence on the relative permeability may be smaller. This needs to be further investigated with dynamic simulations to provide a definite answer.

In general, our work demonstrates that the fluid filling process in heterogeneous porous media is strongly correlated with wetting state and multi-scale pore space structures. The methodologies presented here can be extended to other geological materials for better modelling and simulation of multiphase flow in porous media. Further work is needed to clarify how the mixed wettability distribution obtained with the chemical wettability alteration method used here compares to specific cases in reservoirs and aquifers, including “ageing” by contact with crude oil or non-aqueous phase liquids. This is particularly the case for situations where the alteration takes place on surfaces exposed to oil but not on those exposed to water (Kovscek et al., 1993).

**Acknowledgments**

Shan Wang would like to acknowledge the China Scholarship Council (CSC Grant 201906440157) for PhD support. Tom Bultreys is a postdoctoral fellow of the Research Foundation–Flanders (FWO) and acknowledges its support under grant 12X0919N. The special research fund of the Ghent University (BOF-UGent) is acknowledged for the financial support to the UGCT Centre of Expertise (BOF.EXP.2017.0007). Leonardo Ruspini would like to acknowledge "Norges Forskningrådet" (grant number 296093) for partial support to this research. Arjen Mascini acknowledges funding from the Research Foundation–Flanders (FWO, project G051418N).

**References**

Al-Futaisi, A., & Patzek, T. W. (2004). Secondary imbibition in NAPL-invaded mixed-wet sediments. *Journal of Contaminant Hydrology*, *74*(1–4), 61–81.

Alhammadi, A. M., Gao, Y., Akai, T., Blunt, M. J., & Bijeljic, B. (2020). Pore-scale X-ray imaging with measurement of relative permeability, capillary pressure and oil recovery in a mixed-wet micro-porous carbonate reservoir rock. *Fuel*, *268*(January), 117018. https://doi.org/10.1016/j.fuel.2020.117018

AlRatrout, A., Raeini, A. Q., Bijeljic, B., & Blunt, M. J. (2017). Automatic measurement of contact angle in pore-space images. *Advances in Water Resources*, *109*, 158–169. https://doi.org/10.1016/j.advwatres.2017.07.018

AlRatrout, A., Blunt, M. J., & Bijeljic, B. (2018a). Spatial Correlation of Contact Angle and Curvature in Pore-Space Images. *Water Resources Research*, *54*(9), 6133–6152. https://doi.org/10.1029/2017WR022124

AlRatrout, A., Blunt, M. J., & Bijeljic, B. (2018b). Wettability in complex porous materials, the mixed-wet state, and its relationship to surface roughness. *Proceedings of the National Academy of Sciences of the United States of America*, *115*(36), 8901–8906. https://doi.org/10.1073/pnas.1803734115

583 Andrew, M., Bijeljic, B., & Blunt, M. J. (2014). Pore-scale contact angle measurements at
584 reservoir conditions using X-ray microtomography. *Advances in Water Resources*, *68*,
585 24–31. https://doi.org/10.1016/j.advwatres.2014.02.014

586 Berg, S., Ott, H., Klapp, S. A., Schwing, A., Neiteler, R., Brussee, N., & Makurat, A. (2013).
587 Real-time 3D imaging of Haines jumps in porous media fl ow, *110*(10), 3755–3759.
588 https://doi.org/10.1073/pnas.1221373110

589 Berg, S., Ott, H., Klapp, S. A., Schwing, A., Neiteler, R., Brussee, N., Makurat, A., et al.
590 (2013). Real-time 3D imaging of Haines jumps in porous media flow. *Proceedings of*
591 *the National Academy of Sciences*, *110*(10), 3755–3759.

592 Blunt, M., King, M. J., & Scher, H. (1992). Simulation and theory of two-phase flow in
593 porous media. *Physical Review A*, *46*(12), 7680.

594 Blunt, M. J., Lin, Q., Akai, T., & Bijeljic, B. (2019). A thermodynamically consistent
595 characterization of wettability in porous media using high-resolution imaging. *Journal*
596 *of Colloid and Interface Science*, *552*, 59–65. https://doi.org/10.1016/j.jcis.2019.05.026

597 Brooks, R. H., & Corey, A. T. (1966). Properties of porous media affecting fluid flow.
598 *Journal of the Irrigation and Drainage Division*, *92*(2), 61–88.

599 Buades, A., Coll, B., & Morel, J.-M. (2008). Nonlocal image and movie denoising.
600 *International Journal of Computer Vision*, *76*(2), 123–139.

601 Buckley, J. S., Liu, Y., & Monsterleet, S. (1998). Mechanisms of Wetting Alteration by
602 Crude Oils. *SPE Journal*, *3*(1), 54–61. https://doi.org/10.2118/37230-PA

603 Bultreys, T., Van Hoorebeke, L., & Cnudde, V. (2015). Multi-scale, micro-computed
604 tomography-based pore network models to simulate drainage in heterogeneous rocks.
605 *Advances in Water Resources*, *78*, 36–49.
606 https://doi.org/10.1016/j.advwatres.2015.02.003

607 Bultreys, T., Boone, M. A., Boone, M. N., De Schryver, T., Masschaele, B., Van Loo, D., et
608 al. (2015). Real-time visualization of Haines jumps in sandstone with laboratory-based

microcomputed tomography. *Water Resources Research*, *51*(10), 8668–8676. https://doi.org/10.1002/2015WR017502

Bultreys, T., Boone, M. A., Boone, M. N., De Schryver, T., Masschaele, B., Van Hoorebeke, L., & Cnudde, V. (2016). Fast laboratory-based micro-computed tomography for pore-scale research: Illustrative experiments and perspectives on the future. *Advances in Water Resources*, *95*, 341–351. https://doi.org/10.1016/j.advwatres.2015.05.012

Bultreys, T., Lin, Q., Gao, Y., Raeini, A. Q., Alratrout, A., Bijeljic, B., & Blunt, M. J. (2018). Validation of model predictions of pore-scale fluid distributions during two-phase flow. *Physical Review E*, *97*(5). https://doi.org/10.1103/PhysRevE.97.053104

Burger, W., & Burge, M. J. (2010). *Principles of digital image processing: core algorithms*. Springer Science \& Business Media.

Chen, Y., Jha, N. K., Lebedev, M., An, S., Xie, Q., & Niasar, V. J. (2021). Integral effects of initial fluids configuration and wettability alteration on remaining saturation: characterization with X-ray micro-computed tomography. *Fuel*, *306*, 121717.

Datta, S. S., Ramakrishnan, T. S., & Weitz, D. A. (2014). Mobilization of a trapped non-wetting fluid from a three-dimensional porous medium. *Physics of Fluids*, *26*(2), 22002. https://doi.org/10.1063/1.4866641

Dierick, M., Van Loo, D., Masschaele, B., Van Den Bulcke, J., Van Acker, J., Cnudde, V., & Van Hoorebeke, L. (2014). Recent micro-CT scanner developments at UGCT. *Nuclear Instruments and Methods in Physics Research, Section B: Beam Interactions with Materials and Atoms*, *324*, 35–40. https://doi.org/10.1016/j.nimb.2013.10.051

Gao, Y., Qaseminejad Raeini, A., Blunt, M. J., & Bijeljic, B. (2019). Pore occupancy, relative permeability and flow intermittency measurements using X-ray micro-tomography in a complex carbonate. *Advances in Water Resources*, *129*(April), 56–69. https://doi.org/10.1016/j.advwatres.2019.04.007

Gao, Y., Raeini, A. Q., Selem, A. M., Bondino, I., Blunt, M. J., & Bijeljic, B. (2020). Pore-

scale imaging with measurement of relative permeability and capillary pressure on the same reservoir sandstone sample under water-wet and mixed-wet conditions. *Advances in Water Resources*, *146*(July). https://doi.org/10.1016/j.advwatres.2020.103786

Garfi, G., John, C. M., Lin, Q., Berg, S., & Krevor, S. (2020). Fluid Surface Coverage Showing the Controls of Rock Mineralogy on the Wetting State. *Geophysical Research Letters*, *47*(8), e2019GL086380. https://doi.org/10.1029/2019GL086380

Garing, C., de Chalendar, J. A., Voltolini, M., Ajo-Franklin, J. B., & Benson, S. M. (2017). Pore-scale capillary pressure analysis using multi-scale X-ray micromotography. *Advances in Water Resources*, *104*, 223–241. https://doi.org/10.1016/j.advwatres.2017.04.006

Herring, A. L., Andersson, L., Newell, D. L., Carey, J. W., & Wildenschild, D. (2014). Pore-scale observations of supercritical CO2 drainage in Bentheimer sandstone by synchrotron x-ray imaging. *International Journal of Greenhouse Gas Control*, *25*, 93–101.

Herring, A. L., Middleton, J., Walsh, R., Kingston, A., & Sheppard, A. (2017). Flow rate impacts on capillary pressure and interface curvature of connected and disconnected fluid phases during multiphase flow in sandstone. *Advances in Water Resources*, *107*, 460–469. https://doi.org/10.1016/j.advwatres.2017.05.011

Iglauer, S., Paluszny, A., Pentland, C. H., & Blunt, M. J. (2011). Residual CO2 imaged with X-ray micro-tomography. *Geophysical Research Letters*, *38*(21). https://doi.org/10.1029/2011GL049680

Kalhor, K., Ghasemizadeh, R., Rajic, L., & Alshawabkeh, A. (2019). Assessment of groundwater quality and remediation in karst aquifers: A review. *Groundwater for Sustainable Development*, *8*, 104–121. https://doi.org/10.1016/j.gsd.2018.10.004

Klise, K. A., Moriarty, D., Yoon, H., & Karpyn, Z. (2016). Automated contact angle estimation for three-dimensional X-ray microtomography data. *Advances in Water Resources*, *95*, 152–160. https://doi.org/10.1016/j.advwatres.2015.11.006

662 Kovscek, A. R., Wong, H., & Radke, C. J. (1993). A pore-level scenario for the development
663 of mixed wettability in oil reservoirs. *AIChE Journal*, *39*(6), 1072–1085.

664 Li, T., Schlüter, S., Dragila, M. I., & Wildenschild, D. (2018). An improved method for
665 estimating capillary pressure from 3D microtomography images and its application to
666 the study of disconnected nonwetting phase. *Advances in Water Resources*, *114*, 249–
667 260. https://doi.org/10.1016/j.advwatres.2018.02.012

668 Lin, Q., Al-Khulaifi, Y., Blunt, M. J., & Bijeljic, B. (2016). Quantification of sub-resolution
669 porosity in carbonate rocks by applying high-salinity contrast brine using X-ray
670 microtomography differential imaging. *Advances in Water Resources*, *96*, 306–322.
671 https://doi.org/10.1016/j.advwatres.2016.08.002

672 Lin, Q., Akai, T., Blunt, M. J., Bijeljic, B., Iwama, H., Takabayashi, K., et al. (2021). Pore-
673 scale imaging of asphaltene-induced pore clogging in carbonate rocks. *Fuel*, *283*,
674 118871.

675 Lin, Q., Bijeljic, B., Foroughi, S., Berg, S., & Blunt, M. J. (2021). Pore-scale imaging of
676 displacement patterns in an altered-wettability carbonate. *Chemical Engineering*
677 *Science*, *235*, 116464. https://doi.org/10.1016/j.ces.2021.116464

678 Mascini, A., Cnudde, V., & Bultreys, T. (2020). Event-based contact angle measurements
679 inside porous media using time-resolved micro-computed tomography. *Journal of*
680 *Colloid and Interface Science*, *572*, 354–363. https://doi.org/10.1016/j.jcis.2020.03.099

681 Mascini, A., Boone, M., Van Offenwert, S., Wang, S., Cnudde, V., & Bultreys, T. (2021).
682 Fluid Invasion Dynamics in Porous Media With Complex Wettability and Connectivity.
683 *Geophysical Research Letters*, *48*(22), 1–10. https://doi.org/10.1029/2021GL095185

684 Molenaar, N. (1998). Origin of low-permeability calcite-cemented lenses in shallow marine
685 sandstones and CaCO3 cementation mechanisms: An example from the Lower Jurassic
686 Luxemburg Sandstone, Luxemburg. *Carbonate Cementation in Sandstones: Distribution*
687 *Patterns and Geochemical Evolution*, 193–211.

688 Morrow, N. R. (1990). Wettability and its effect on oil recovery. *JPT, Journal of Petroleum*
689 *Technology*, *42*(12), 1476–1484. https://doi.org/10.2118/21621-PA

690 Offenwert, S. Van. (2019). Pore - Scale Visualization and Quanti fi cation of Transient
691 Solute Transport Using Fast Microcomputed Tomography Water Resources Research,
692 9279–9291. https://doi.org/10.1029/2019WR025880

693 Panfilov, M. (2010). Underground Storage of Hydrogen: In Situ Self-Organisation and
694 Methane Generation. *Transport in Porous Media*, *85*(3), 841–865.
695 https://doi.org/10.1007/s11242-010-9595-7

696 Reynolds, C. A., Menke, H., Andrew, M., Blunt, M. J., & Krevor, S. (2017). Dynamic fluid
697 connectivity during steady-state multiphase flow in a sandstone. *Proceedings of the*
698 *National Academy of Sciences of the United States of America*, *114*(31), 8187–8192.
699 https://doi.org/10.1073/pnas.1702834114

700 Rücker, M., Berg, S., Armstrong, R. T., Georgiadis, A., Ott, H., Schwing, A., et al. (2015).
701 From connected pathway flow to ganglion dynamics. *Geophysical Research Letters*,
702 *42*(10), 3888–3894. https://doi.org/10.1002/2015GL064007

703 Ruspini, L. C., Øren, P. E., Berg, S., Masalmeh, S., Bultreys, T., Taberner, C., et al. (2021).
704 Multiscale Digital Rock Analysis for Complex Rocks. *Transport in Porous Media*,
705 *139*(2), 301–325. https://doi.org/10.1007/s11242-021-01667-2

706 Scanziani, A., Singh, K., Blunt, M. J., & Guadagnini, A. (2017). Automatic method for
707 estimation of in situ effective contact angle from X-ray micro tomography images of
708 two-phase flow in porous media. *Journal of Colloid and Interface Science*, *496*, 51–59.
709 https://doi.org/10.1016/j.jcis.2017.02.005

710 Scanziani, A., Lin, Q., Alhosani, A., Blunt, M. J., & Bijeljic, B. (2020). Dynamics of fluid
711 displacement in mixed-wet porous media. *Proceedings of the Royal Society A*,
712 *476*(2240), 20200040.

713 Shukla, R., Ranjith, P., Haque, A., & Choi, X. (2010). A review of studies on CO2

714 sequestration and caprock integrity. *Fuel*, *89*(10), 2651–2664.
715 https://doi.org/10.1016/j.fuel.2010.05.012

716 Singh, K., Bultreys, T., Raeini, A. Q., Shams, M., & Blunt, M. J. (2022). New type of pore-
717 snap-off and displacement correlations in imbibition. *Journal of Colloid and Interface*
718 *Science*, *609*, 384–392. https://doi.org/10.1016/j.jcis.2021.11.109

719 Soulaine, C., Gjetvaj, F., Garing, C., Roman, S., Russian, A., Gouze, P., & Tchelepi, H. A.
720 (2016). The impact of sub-resolution porosity of X-ray microtomography images on the
721 permeability. *Transport in Porous Media*, *113*(1), 227–243.

722 Spurin, C., Bultreys, T., Bijeljic, B., Blunt, M. J., & Krevor, S. (2019). Intermittent fluid
723 connectivity during two-phase flow in a heterogeneous carbonate rock. *Physical Review*
724 *E*, *100*(4), 1–10. https://doi.org/10.1103/PhysRevE.100.043103

725 Sun, C., McClure, J. E., Mostaghimi, P., Herring, A. L., Meisenheimer, D. E., Wildenschild,
726 D., et al. (2020). Characterization of wetting using topological principles. *Journal of*
727 *Colloid and Interface Science*, *578*, 106–115.

728 Wang, S., Ruspini, L. C., Øren, P. E., Van Offenwert, S., & Bultreys, T. (2022). Anchoring
729 Multi-Scale Models to Micron-Scale Imaging of Multiphase Flow in Rocks. *Water*
730 *Resources Research*, *58*(1), 1–16. https://doi.org/10.1029/2021WR030870

731 Zankoor, A., Khishvand, M., Mohamed, A., Wang, R., & Piri, M. (2021). In-situ capillary
732 pressure and wettability in natural porous media: Multi-scale experimentation and
733 automated characterization using X-ray images. *Journal of Colloid and Interface*
734 *Science*, *603*, 356–369.

735 Zhang, X., Crawford, J. W., Flavel, R. J., & Young, I. M. (2016). A multi-scale Lattice
736 Boltzmann model for simulating solute transport in 3D X-ray micro-tomography images
737 of aggregated porous materials. *Journal of Hydrology*, *541*, 1020–1029.

738